

pubs.acs.org/cm Article

Tunable Atomic Layer Deposition into Ultra-High-Aspect-Ratio (>60000:1) Aerogel Monoliths Enabled by Transport Modeling

Andrew J. Gayle,[#] Zachary J. Berquist,[#] Yuxin Chen, Alexander J. Hill, Jacob Y. Hoffman, Ashley R. Bielinski, Andrej Lenert,* and Neil P. Dasgupta*



ACCESS I

Cite This: Chem. Mater. 2021, 33, 5572–5583



Article Recommendations

ABSTRACT: Atomic layer deposition (ALD) modification of ultra-high-aspect-ratio structures (>10000:1) is a powerful platform with applications in catalysis, filtration, and energy conversion. However, the deposition of conformal and tunable ALD coatings at these aspect ratios remains challenging, resulting in empirical trade-offs between the precursor utilization and reaction time. Here, we demonstrate tunable control of the ALD infiltration depth into an aerogel monolith (AM) and develop a reaction-diffusion model to accurately describe the coating process.

Specifically, we investigate the ALD exposure time and precursor dose needed to conformally coat a silica AM with pore sizes of \sim 20

nm, a monolith thickness of \sim 2.5 mm, and aspect ratios exceeding 60000:1. We demonstrate complete infiltration into the AM, which

III Metrics & More

Mapping ALD into Aerogel Monolith

Precursor

All Model of Coating Process

Model Validation

Precursor

All Model of Coating Process

Model Validation

Model of Coating Process

Exposure Time (s)

s Supporting Information

is quantified by elemental mapping. A reaction-diffusion model is developed, which accounts for multiple doses and the precursor depletion in the ALD chamber during an exposure step. The experimentally validated model enables the prediction and tuning of infiltration depth into a tortuous, high-aspect-ratio structure such as an AM, allowing for the synthesis of rationally designed material architectures. Additionally, the model allows for co-optimization of the total deposition time and percentage of unreacted precursor, which are important for the manufacturability and sustainability of ALD processing. Lastly, we demonstrate that ultrathin ALD Al_2O_3 coatings can be used to stabilize silica AMs against structural degradation under high-temperature annealing conditions (700–800 °C) by limiting changes in the surface area and monolith volume. This improved high-temperature stability has implications for numerous aerogel applications, including catalysis and thermal insulation.

■ INTRODUCTION

Aerogels are versatile materials used in a variety of applications, 1,2 including but not limited to catalysis, 3 thermal insulation, filtration, and Cherenkov radiation. Aerogels have high specific surface areas, low densities, and small pore sizes, generally on the order of 1-100 nm. They can be fabricated via sol-gel synthesis, often using a supercritical drying step to preserve the mesoporous structure. Most aerogels are currently composed of a single binary oxide (e.g., silica) or a carbonaceous material; however, this limits the range of potential aerogel material properties and applications. Surface modifications during sol-gel synthesis, including hydrophobization and growth of inorganic capping layers, have been reported but are typically unstable at temperatures >250 °C and result in the degradation of aerogel structural and optical properties, respectively. Therefore, there is a strong motivation to develop new methods to alter the surface chemistry of aerogels while maintaining the ease of synthesis afforded by well-established sol-gel chemistry.

One strategy to modulate the surface chemistry of aerogels is coating with a secondary material after supercritical drying. However, such surface modifications are complicated by the high-aspect-ratio internal pore structure, eliminating the use of line-of-sight techniques such as sputtering or evaporation. Liquid-phase surface modifications can be complicated by the pore collapse due to capillary forces in the nanoscale aerogel pores and slow diffusion. Efforts have been made to address these limitations: atomic layer deposition (ALD) is a powerful vapor-phase deposition technique that is suitable for conformally coating ultra-high-aspect-ratio structures because of its self-limiting surface reactions and subnanometer control of material thickness and composition. ^{9,10}

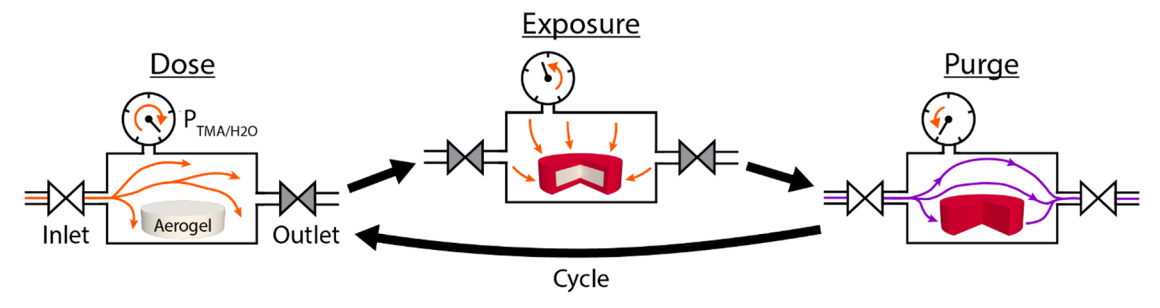
ALD has been used to deposit conformal thin films or nanoparticle islands onto the surfaces of a variety of high-aspect-ratio structures, including silicon trenches, 11,12 anodic

Received: March 2, 2021 Revised: June 21, 2021 Published: July 9, 2021





Scheme 1. Schematic of the Reactor Conditions during a QSM Recipe^a



"Dose step: The precursor is dosed into the chamber with the outlet valve closed. Exposure step: The precursor diffuses into the AM to a desired depth without pumping or purging. Purge step: The reactor is flushed with Ar, removing any remaining reactant and product species. In the multidose-QSM process used in this study, the same precursor (e.g., trimethylaluminum, TMA) is dosed, exposed, and purged multiple times before the counter reactant is introduced. By the end of the QSM process, the AM has been coated to a desired infiltration depth.

alumina (AAO), ^{13,14} track-etched polycarbonate membranes, ¹⁵ nanowires, ^{16,17} carbon nanotubes, ¹⁸ lateral high-aspect-ratio (LHAR) structures, ^{19,20} and others. Owing to the wide range of materials that can be deposited by ALD, ^{21,22} including but not limited to metal oxides, nitrides, sulfides, and elemental metals, conformal surface modifications on these high-aspectratio structures offer a wide degree of versatility in material properties.

Early reports of ALD on aerogels focused on Al₂O₃ and ZnO coatings on silica aerogels.²³ ALD-coated aerogels have been subsequently used for a variety of applications, including dyesensitized solar cells, ^{24–26} battery electrodes, ^{27–29} water purification, ^{30,31} and catalysis. ^{32–36} Characterization of ALD coatings on aerogels has been performed using high-resolution microscopy, 37,38 mass gain and surface area measurements, 36 and elemental mapping on the tens-to-hundreds of micrometers scale.^{39,40} However, despite these promising examples, evidence of ALD conformality on millimeter scale, ultra-highaspect-ratio aerogel monoliths (AMs) is scarce in the literature. To our knowledge, no papers have quantitatively demonstrated ALD conformality on aerogels with aspect ratios greater than 5000:1.39,40 In this study, we demonstrate a process for coating ultra-high-aspect-ratio (>60000:1) AMs, which can enable the use of millimeter-scale aerogels as "bulk" materials in new application spaces such as concentrated solar thermal (CST) technologies, thermal insulation, and catalysis. This experimentally measured, ALD-coated aspect ratio is more than an order of magnitude greater than any previous report of ALD on aerogel substrates.

To understand the ALD coating process on high-aspect-ratio structures and determine the processing conditions needed for conformal coverage, a variety of models have been developed, including analytical/continuum approaches, 39,41-43 kinetic Monte Carlo simulations, 13,44 ballistic simulations, 45 and multiscale modeling. 46-48 A recent review by Cremers et al. as well as a book by Yanguas-Gil provide comprehensive overviews of many of these efforts. 9,49 Well-defined highaspect-ratio structures, such as LHAR structures and AAO, are often used to experimentally measure ALD infiltration and assist in the development of diffusion and reaction models. 13,19,20 The analytical model by Gordon et al. has been used extensively and offered a starting point for numerous other efforts. 41 This model predicts a necessary precursor exposure, defined by the product of the exposure time and precursor partial pressure in the deposition chamber, which is necessary to coat a structure of a specific aspect ratio.

Key assumptions in the model include a constant precursor partial pressure in the reaction chamber as well as a binary reaction probability of 1 on unreacted sites and 0 on already-reacted sites. This results in an abrupt ALD coating front in the structure. Yanguas-Gil and Elam subsequently developed a model that includes a nonbinary reaction probability that allows for a partially coated gradient at the coating front. Additionally, Jin et al. performed numerical simulations of ALD infiltration into random, tortuous nanoparticle agglomerates. Studies by Lankhorst et al. and Miyano et al. modeled the transient depletion of the precursor concentration in the reaction chamber in a constant-flow ALD process. Grillo et al. modeled ALD on nanoparticles and micrometer-scale nanoporous particles in a fluidized-bed reactor to optimize precursor utilization.

Despite the variety of approaches used in previous studies, most modeling efforts to date have considered continuous flow and purging of ALD precursors. This can lead to undesirably long time scales and/or inefficient precursor utilization to achieve conformal coatings on aspect ratios >10000:1 in nanoporous templates. To overcome these limitations, quasistatic mode (QSM) strategies can be utilized, that is, introducing a precursor into an ALD reaction chamber without continuous purging and pumping. QSM strategies have been implemented in ALD on a variety of substrates, including AAO, annotubes, annoporous polymer membranes, metal organic frameworks (MOFs), among others. Although it is a commonly used technique, an accurate model of the ALD process under QSM conditions on high-aspect-ratio structures is currently lacking. Specifically, the impacts of (1) precursor depletion in the ALD chamber during an exposure step and (2) multiple precursor doses before dosing the counter reactant have not been previously described. Current constant-flow ALD models are not suitable for accurately representing QSM procedures because of assumptions inherent in the models, involving constant precursor partial pressures in the chamber and a pair of single precursor doses per ALD cycle. Therefore, in this study, we develop a model of QSM deposition processes that can be used to co-optimize deposition time and the percentage of wasted precursor when coating ultra-high-aspect-ratio structures.

Herein, we demonstrate conformal ALD coatings on millimeter-scale silica AMs with aspect ratios >60000:1 while maintaining ideal, self-limiting ALD behavior. We describe the ALD coating process using an experimentally validated analytical model, which includes precursor partial pressure

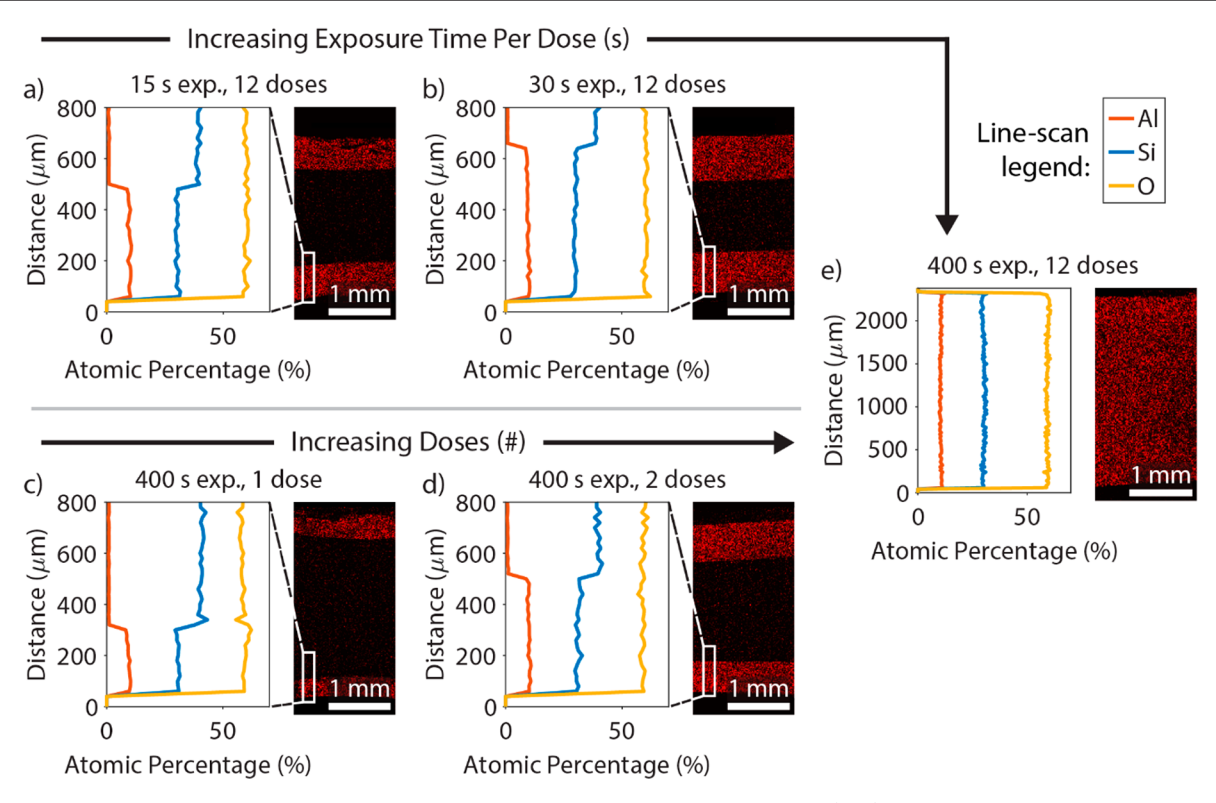


Figure 1. SEM/EDS elemental mapping and line scans of cross sections of ALD-coated AMs. (a, b) Varying the exposure time per dose while holding fixed 12 precursor doses of TMA and DI water, (c, d) varying the number of precursor doses while holding fixed 400 s of exposure time per dose, and (e) conformally coated AM. In each of the EDS maps and line scans, the concave side of the AM is at the top of the image, and the AM cylinder was sectioned along the circumference into four equally sized pieces prior to deposition (details in Supplementary Note #5).

changes in the reaction chamber during a QSM exposure, as well as the effects of multiple doses of a single precursor. This model enables the prediction and subsequent tuning of infiltration depth into a high-aspect-ratio material, allowing for the synthesis of rationally designed structures with versatile material properties. While AMs are the focus of this study, they serve as a model system for a general class of mesoporous substrates. The model developed herein is thus applicable to OSM approaches on other high-aspect-ratio structures, as well as sequential vapor infiltration (SVI) into polymeric materials. In this study, we demonstrate the effects of an ALD Al₂O₃ coating on the structural stability of silica AMs during hightemperature annealing, characterized by changes in the AM size and surface area. One cycle of ALD modification improves the thermal stability window of silica aerogels from ~ 600 °C⁵⁵ to beyond 700 °C, expanding the possible use cases for aerogels in high-temperature applications such as CST and heterogeneous catalysis.

■ RESULTS AND DISCUSSION

ALD Multidose-Quasi-Static Mode. To conformally coat silica AMs, we implement an ALD procedure known as QSM (alternatively referred to as "exposure mode")¹³ (Scheme 1). In a single QSM exposure, ALD precursors are dosed into the reaction chamber without active pumping or purging. An example pressure profile for a QSM recipe is shown in the Supporting Information (Figure S1).

Owing to the high surface area of the AM and the correspondingly large amount of precursor necessary to saturate the aerogel surface, a multidose-QSM recipe is implemented (Figure S2). In this recipe, a single precursor is

sequentially dosed, exposed, and purged multiple times before dosing the counter reactant. This approach allows for replenishment of the depleted precursor partial pressure during sequential doses, which decreases the time required for complete infiltration of the AM compared to using a single exposure step. An analogous strategy has been implemented in the field of vapor phase infiltration (VPI), ⁵⁶ which is a process in which precursors diffuse into and react inside bulk polymers. SVI is a subcategory of VPI, which uses multiple doses of a single precursor before dosing the counter reactant. ^{57–59} SVI can be used to overcome reactant supply limitations and promote precursor saturation, which is often quantified by mass gain measurements. ^{57,58}

In the multidose-QSM procedure, purging is performed after each exposure step to remove product species and enable sufficient dosage of the precursor in the following dose step. The total precursor dose introduced into the chamber was fixed for each exposure, followed by a variable exposure time. At the beginning of an individual exposure step, the precursor ($P_{\rm TMA/H_2O} \geq 17$ Torr, Supplementary Notes #3 and #4 in the Supporting Information) constituted a majority of the partial pressure in the chamber ($P_{\rm Ar} < 1$ Torr). The TMA and deionized (DI) water precursor sources were kept at 37 °C to slightly boost their vapor pressures.

In this study, one complete ALD cycle was performed in each experiment. In standard ALD recipes, one cycle consists of (1) dosing/exposing precursor A, (2) purging excess precursor A and reaction products, (3) dosing/exposing precursor B, and (4) purging excess precursor B and reaction products. In the case of multidose-QSM in this study, steps 1

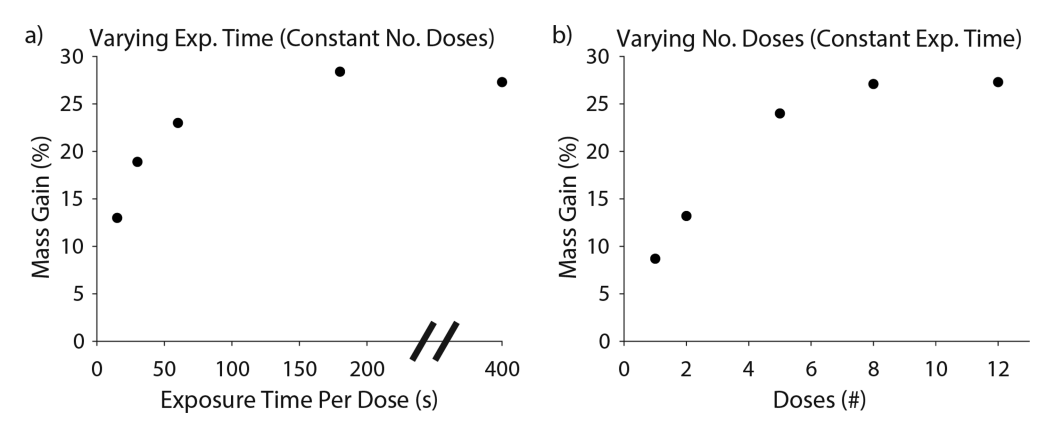


Figure 2. Mass gain measurements of ALD-coated AMs to study the saturation behavior. Percentage gain was measured relative to the initial, uncoated AM mass. (a) Varying exposure time per dose using 12 precursor doses of TMA and DI water, and (b) varying number of precursor doses using 400 s of exposure time per dose.

and 2 are repeated multiple times prior to steps 3 and 4, which are also repeated the same number of times.

ALD Infiltration Depth into Aerogel Monoliths. The exposure time per dose and total number of precursor doses were independently varied to decouple the effects of these parameters on the ALD infiltration depth into the AM (Figure 1). As shown in Figure 1a,b, even when a sufficiently large number of precursor doses were used to coat the entire monolith, short exposure times per dose hinder infiltration into the AM, primarily because of diffusion limitations. Depositions using a low number of precursor doses with long exposure times per dose, as shown in Figure 1c,d, have similarly low infiltration depths into the monolith. The entire AM can only be fully and conformally coated by using a sufficiently large number of precursor doses and long exposure times per dose (Figure 1e).

The accompanying scanning electron microscopy/energy-dispersive X-ray spectroscopy (SEM/EDS) line scans in Figure 1 show the atomic percentages of Al, Si, and O with respect to distance from the surface of the AM. The coated regions of the AM cross sections exhibit a constant atomic percentage of Al (10 ± 1.5 at. %). This indicates that these regions have experienced self-limiting surface reactions with the precursor, as the atomic percentage of Al does not continue to increase with respect to the exposure time per dose or number of doses.

Surface saturation is an important aspect of every ALD process. ^{9,10,60} In most studies on planar substrates, saturation is evaluated by varying the pulse and/or exposure times of the precursors and measuring the thickness increase per cycle. ^{10,11} Alternatively, in the case of a sufficiently high surface area substrate, the total mass gain after ALD can also be measured *ex situ* and used to evaluate saturation behavior. ⁶¹ Here, we apply this second approach to confirm the self-limiting nature of a single ALD cycle throughout the bulk AM volume under multidose-QSM.

In Figure 2, the mass gain of a series of AM samples with varying exposure times and number of doses is shown. To minimize the effects of water adsorption, the initial mass of the AM was measured after the sample was allowed to dry under vacuum for at least 1 h at 150 $^{\circ}$ C. The ALD-coated AM mass was measured using an analytical balance within 1–2 min after removal from the ALD chamber. The initial AM mass was \sim 75 mg. The mass gain is shown to initially increase with respect to the exposure time per dose and the number of doses and eventually saturate at \sim 27%. Under these saturated conditions,

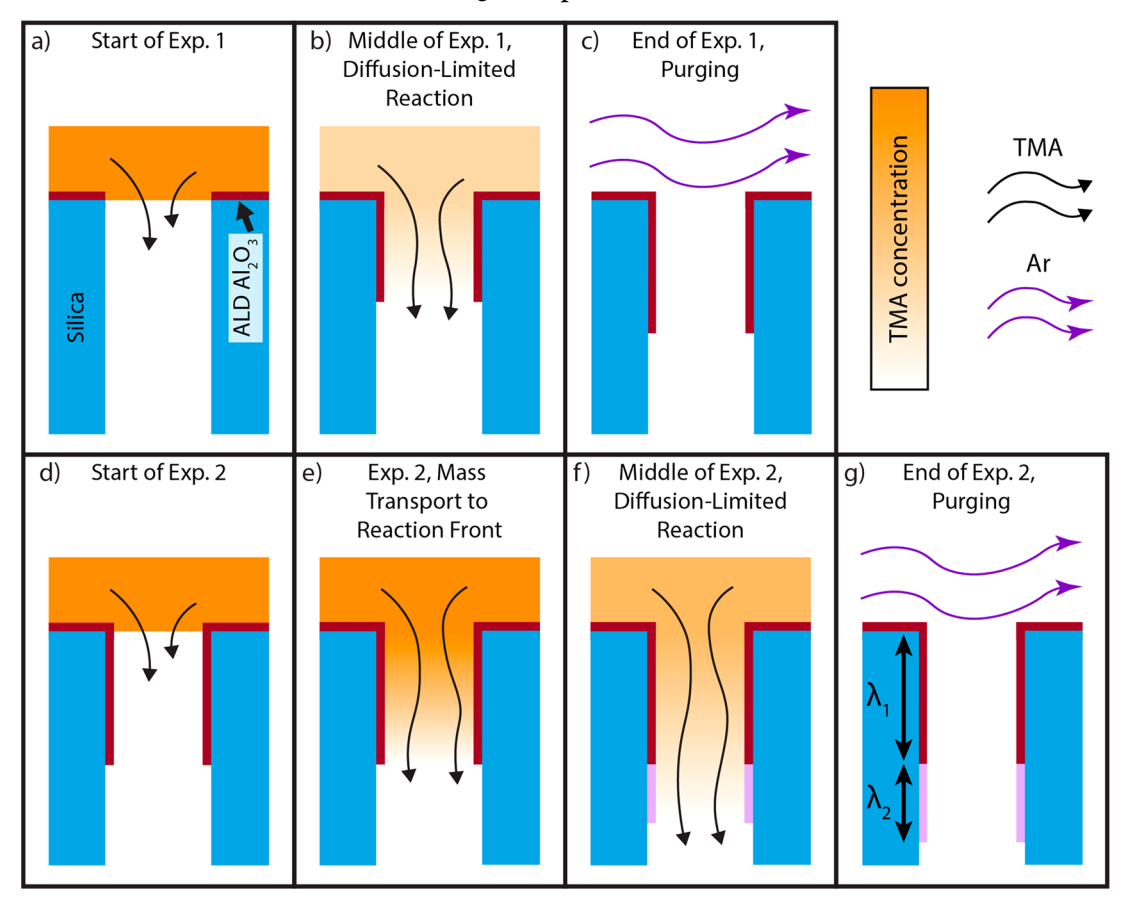
the AM is fully coated by ALD, as shown in Figure 1e. Importantly, further increases in either the exposure time per dose or the number of doses does not result in a further increase in the mass gain, demonstrating saturation and self-limiting behavior in the ALD process.

The expected saturated mass gain after complete coating of the AM can be approximated using the AM specific surface area, ALD thickness growth per cycle, and Al₂O₃ density. Detailed calculations can be found in the Supporting Information (Supplementary Note #7). The theoretically predicted mass gain value of ~38% after complete coating is slightly higher than the measured value of \sim 27%. Furthermore, the expected atomic composition percentage of Al can be calculated using the trimethylaluminum (TMA) saturation dose, that is, the number of TMA molecules that can chemisorb per substrate surface area (Supplementary Notes #7 and #8). After one conformal ALD cycle, the predicted Al atomic percentage is 13%, which is slightly higher than the experimental value of ~10% in the ALD-saturated regions of the AMs (Figure 1). The differences in both of these predictions could be attributed to several factors, including differences in the saturated growth per cycle and density during the first ALD cycle compared to steady-state growth values based on measurements of "bulk" ALD films after >100 cycles (Supplementary Note #7). Overall, these theoretical calculations are in good agreement with the observed saturation trends in Figure 2.

Based on the EDS line scans in Figure 1, the infiltration depth with respect to exposure time per dose and number of doses can be measured (Supplementary Note #9). In the following section, these data are used to calibrate a model of the multidose-QSM ALD process on ultra-high-aspect-ratio structures.

Model of Multidose-QSM Process. Our ALD coating model is adapted from the analytical model of ALD on high-aspect-ratio structures by Gordon et al. The Gordon model assumes diffusion-limited mass transport. The flux of precursor molecules into the structure is treated similarly to a "vacuum pump" with gases in the molecular flow regime, where the vacuum source is the deeper, uncoated portion of the pore (further details can be found in ref 41). Furthermore, it assumes a constant precursor partial pressure outside of the structure's pores and no mass-transport limitations to the edge of the pore. Molecular diffusion is assumed within the pore, where precursors interact only with the pore walls. The

Scheme 2. Visualization of the First Two Multidose-QSM Steps^a



"A single, straight pore is shown for clarity. (a) The precursor has not diffused into the structure. (b) The precursor is diffusing into and reacting with the structure. (c) The unreacted precursor is purged away. (d) The precursor must diffuse to the ALD reaction front before reacting. (e) The re-establishment of pseudo-steady-state diffusion in exposure 2. The precursor begins reacting with the structure. (f) The precursor is diffusing into and reacting with the structure. (g) The unreacted precursor is purged away.

likelihood of a precursor molecule chemisorbing with a surface site upon collision (i.e., reaction probability) is assumed to be binary, where a value of 1 is applied to sites that have not reacted with a precursor molecule, and a value of 0 is applied to sites that have reacted with a precursor molecule. The Gordon model assumes straight pores, so no tortuosity is included. Using these assumptions, the precursor flux J [1/m²/s] at the ALD-coated front, located at a depth of λ [m], is defined as the impingement flux on a flat surface modified by the Clausing factor: 62

$$J = \frac{P}{(2\pi mkT)^{1/2} \left(1 + \frac{3\lambda p}{16A}\right)}$$
 (1)

where P [Pa] is the precursor partial pressure immediately outside of the pore entrance, m [kg] is the mass of one precursor molecule, k is the Boltzmann constant [1.38 \times 10⁻²³ J/K], T [K] is the deposition temperature, p [m] is the pore perimeter, and A [m²] is the pore cross-sectional area. When the change in coating depth with time is solved, the exposure required for complete coverage of the walls of the structure can be determined as

$$Pt = S(2\pi mkT)^{1/2} \left[4a + \frac{3}{2}a^2 \right]$$
 (2)

where t [s] is the exposure time, S [1/m²/s] is the precursor saturation dose, a = Lp/4A is the aspect ratio, and L [m] is the length of the pore.

Yanguas-Gil et al. developed a model that incorporates a nonbinary precursor reaction probability, which captures the gradient in precursor chemisorption at the coating front. In cases with a sufficiently high reaction probability or aspect ratio, the necessary dose in the Yanguas-Gil model simplifies to a quadratic dependence on aspect ratio, similar to eq 2. When considering the ultra-high-aspect-ratio AMs that were investigated in this work, the effect of including a nonbinary reaction probability was found to be negligible (Supplementary Note #10).

Although the Gordon and Yanguas-Gil models describe an ALD process that has a single exposure step with negligible precursor depletion in the reaction chamber, additional considerations are necessary to describe the multidose-QSM procedure used in this study. To this end, we developed a deposition model to account for precursor depletion in the chamber during an exposure step, as well as the use of multiple doses of a single precursor before dosing the counter reactant.

While a complete set of assumptions and justifications in the multidose-QSM model is provided in the Supporting Information, a few key assumptions are presented here. Precursor diffusion inside the AM pores is modeled in the molecular flow regime, whereas external transport limitations

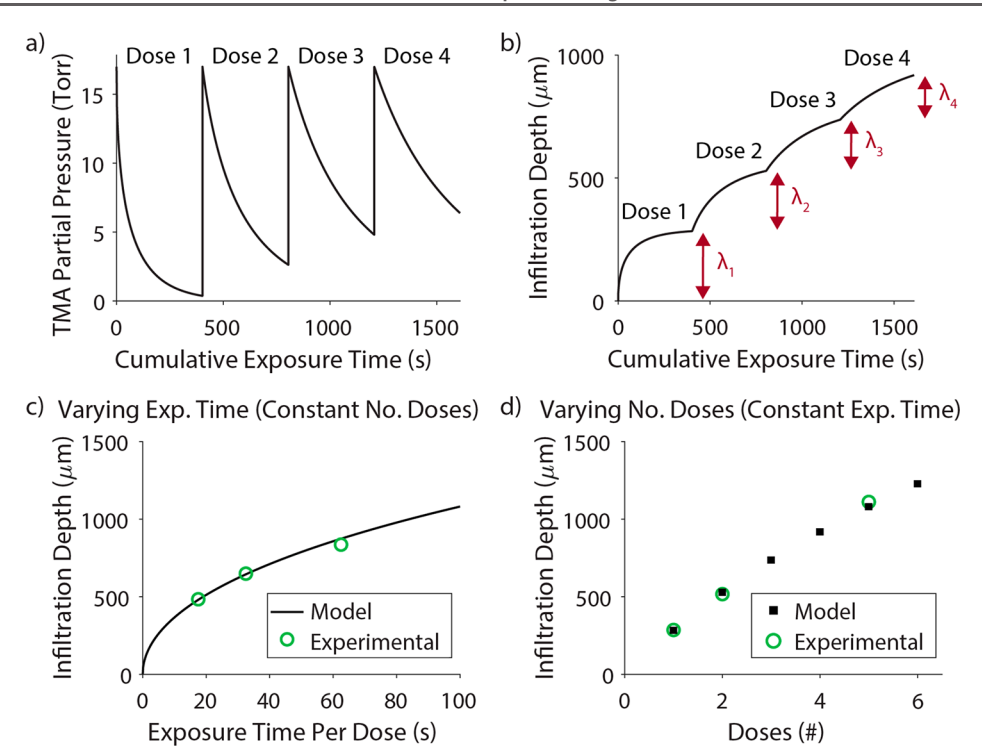


Figure 3. Results of multidose-QSM ALD process model and experimental data comparison. (a) Modeled TMA partial pressure in the reaction chamber and (b) ALD infiltration depth with respect to cumulative exposure time for a recipe with 4 doses of TMA and an exposure time per dose of 400 s. (c) ALD infiltration depth using 12 TMA doses with varying exposure times per dose. (d) ALD infiltration depth for a varying number of TMA doses, each with an exposure time per dose of 400 s.

in the chamber are neglected. Validations of these assumptions are provided in Supplementary Notes #3 and #4. A onedimensional (1D) model is used because of the large AM diameter relative to its thickness (>5:1). TMA dosing is assumed to be the rate-determining step in the ALD process because of its lower vapor pressure and diffusion coefficient compared to DI water, and its lower diffusion coefficient compared to species present (Ar, CH₄) during purging (Supplementary Note #3). The aerogel pore cross section is considered to be circular on average, with a diameter of ~22 nm, which was calculated on the basis of Brunauer-Emmett-Teller (BET) measurements (Supplementary Note #11). While straight pores were considered in the Gordon model, AMs contain a random, tortuous network of pores. This is taken into account in our model using the tortuosity, defined as the ratio of the path length through the AM compared to the measured AM thickness.

The multidose-QSM procedure is depicted in Scheme 2. In the first exposure step, the precursor is dosed into the chamber (Scheme 2a) and begins diffusing into the AM (Scheme 2b). The precursor reaction within the AM occurs at the ALD-coated reaction front, taking the form of a step function because of the binary reaction coefficient. With use of the tortuosity τ , the expression for the precursor flux at the ALD-coated reaction front in the Gordon model (eq 1) is modified as

$$J = \frac{P}{\tau (2\pi mkT)^{1/2} \left(1 + \frac{3\lambda p}{16A}\right)}$$
 (3)

After a differential time step (dt), this flux results in a change in the ALD infiltration depth (d λ) as

$$dt = \frac{SB}{J} d\lambda \tag{4}$$

where $B\ [\mathrm{m^2/m^3}]$ is the volumetric surface area of the AM. Owing to the hierarchical nature of the aerogel porosity, multiple pore length scales must be considered when modeling the complete coverage of the ALD coating. Specifically, there is a large fraction of relatively small mesopores (2–50 nm in diameter) that do not contribute significantly to diffusion deep into the AM, but still must be coated in a conformal ALD process. Therefore, the volumetric surface area is used instead of a single-pore surface area to separate the average pore size (which is necessary for flux/diffusion calculations) from the total surface area available for deposition.

The quantity of precursor that is consumed during a differential time step can be calculated from the flux at the ALD-coated front and the ideal gas law as follows:

$$JA_0\phi = \frac{\mathrm{d}N}{\mathrm{d}t} = \frac{\left(\frac{\mathrm{d}P}{\mathrm{d}t}\right)VN_{\mathrm{v}}}{RT} \tag{5}$$

where A_0 [m²] is the projected surface area of the AM, ϕ is the porosity, N [1/m³] is the precursor concentration in the chamber, V [m³] is the volume of the chamber, $N_{\rm v}$ [1/mol] is Avogadro's number, and R [J/mol/K] is the ideal gas constant. During the first exposure step, eqs 3–5 can be solved numerically when using a sufficiently small time step, in this case 1 ms.

After the first exposure step, the depth of the ALD coating inside the structure (λ_1) is calculated on the basis of the exposure time and initial precursor dose. The remaining precursor and any reaction products are purged from the chamber (Scheme 2c), and the second dose is supplied

(Scheme 2d). At the start of the second dose, there is no precursor within the pores. Diffusion from the chamber to the reaction front must occur. During this step, the precursor concentration field is re-equilibrated rapidly compared to the time needed to change the diffusion path length (Scheme 2e). This can be appreciated by noting that the average velocity of the reaction front $(d\lambda/dt)$ is approximately 5×10^{-4} mm/s (Figure 3b), whereas the characteristic velocity associated with precursor diffusion to the front (D_{eff}/λ) is 1 mm/s, where D_{eff} is the effective diffusion coefficient of the precursor within the pore (see Supplementary Notes #3 and #12). Similarly, a steady-state concentration profile of the product species (CH₄) is also established relatively fast. Thus, to excellent accuracy, transport can be modeled by pseudo-steady-state diffusion to the moving reaction front, represented by eqs 3-5. We note that the relatively slow velocity of the reaction front is a consequence of the large volumetric surface of the aerogel pores, as discussed above. The overall mass-transport rate is, thus, controlled by pseudo-steady-state diffusion through the long, tortuous pores, and not by the precursor reaction rate.

The model outputs are shown in Figure 3. The TMA partial pressure in the chamber (Figure 3a) is displayed with respect to cumulative exposure time. The partial pressure decreases with respect to time in each individual exposure step because of precursor consumption by reaction sites within the AM (Scheme 2b,f). At the end point of each sequential 400 s exposure step, the partial pressure of TMA remaining in the chamber monotonically increases. This illustrates that the percentage of precursor used to coat the AM is very high in the first dose, but it decreases in subsequent doses.

Figure 3b shows the model results for the incremental increase in infiltration depth (λ_{1-4}) , which decreases with each subsequent dose. The reason for this trend is that the precursor molecules must diffuse progressively deeper into the AM to supply the necessary reactant flux (Scheme 2c,g). Consequently, precursor utilization decreases with each subsequent exposure step (Figure 3a).

In this model, the tortuosity (τ) is treated as a fitting parameter, owing to the difficulty in experimentally evaluating this value in a random aerogel network. A tortuosity of 1.8 yielded good agreement between the modeled and experimentally measured infiltration depths (Figure 1) for a series of recipes with varying exposure times per dose (Figure 3c) and number of doses (Figure 3d). This tortuosity is consistent with previous publications on aerogels and other substrates with similar porosities and pore sizes. ^{63–65} A sensitivity analysis was performed on the fitted tortuosity (τ) for values between 1.5 and 2.1 (Supplementary Note #13). Although the modeled infiltration depths vary slightly depending on τ , the trends are consistent regardless of the exact value. We note that experimental infiltration depths are accurate to $\sim 20 \ \mu m$ because of the data point spacing in the SEM-EDS measurements. This corresponds to an uncertainty in the fitted tortuosity of ≤ 0.1 .

The agreement between the modeled and experimental data enables the prediction of the process parameters necessary to reach a certain infiltration depth into an AM. Although the exact deposition conditions presented here are a function of the reactor volume as well as the substrate and precursor properties, the model allows for generalization to an arbitrary reactor, deposition process, and substrate geometry. This framework is important for the efficient development of new ALD processes on ultra-high-aspect-ratio substrates.

The model further allows for the quantification of important ALD process characteristics, including the total processing time (Figure 4). The total processing time is defined as the

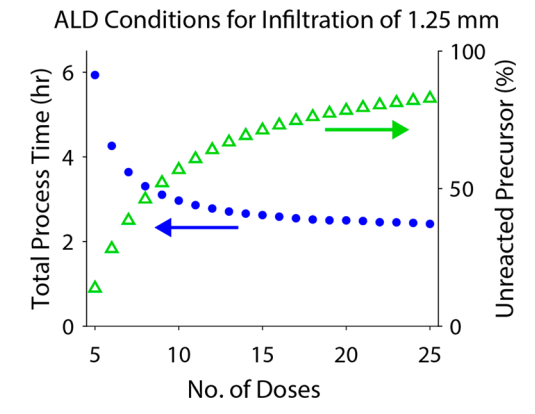


Figure 4. ALD process efficiency trade-offs using the multidose-QSM model. Total processing time (h) and percentage of unreacted precursor (%) are calculated with respect to number of doses. The final infiltration depth for each of these conditions is maintained at 1.25 mm by adjusting the exposure time per dose (e.g., 5 doses, 712 s; 10 doses, 178 s; 15 doses, 105 s; 20 doses, 75 s; 25 doses, 58 s). The initial bakeout and water precycle times are not included in the total processing time.

sum of all exposure and purge times. To achieve a fixed infiltration depth (1.25 mm) using the multidose-QSM method, increasing the total number of doses enables a lower exposure time per dose. This results in a lower total processing time, decreasing from greater than 5.5 h to less than 3 h when the total number of doses increases from 5 to 25.

This observation can be rationalized by the fact that when the number of doses increases and the exposure time per dose decreases, the precursor partial pressure in the ALD chamber decreases less significantly during each exposure step (Supplementary Note #14). When a very large number of doses are used, the process approaches a constant-flow regime, where depletion of the precursor in the reaction chamber is negligible. Maintaining constant precursor partial pressure in the chamber helps to mitigate diffusion limitations. However, as shown in Figure 4, there are diminishing returns in terms of limiting the total processing time when increasing the number of doses and decreasing the exposure time per dose.

In addition to total processing time, the percentage of unreacted precursor can also be calculated (Figure 4). When a low number of doses and a very long exposure time per dose are used, nearly all of the precursor in the chamber has time to diffuse into and react with the AM, resulting in low levels of wasted precursor (<30%). Alternatively, when the regime of constant precursor partial pressure in the chamber is approached, large amounts of precursor are not utilized (because of the necessary short exposure times per dose) and are thus purged directly into the vacuum pump. This results in precursor waste levels exceeding 80%. After evaluation of the trade-off between total processing time and percentage of unreacted precursor in Figure 4, we selected \sim 12 precursor doses to fully coat the samples used in Figures 1–4.

In this study, we implemented a constant exposure time per dose in each individual deposition recipe. As an alternative strategy, increasing the exposure time during later doses can enable further tuning of the percentage of unreacted precursor

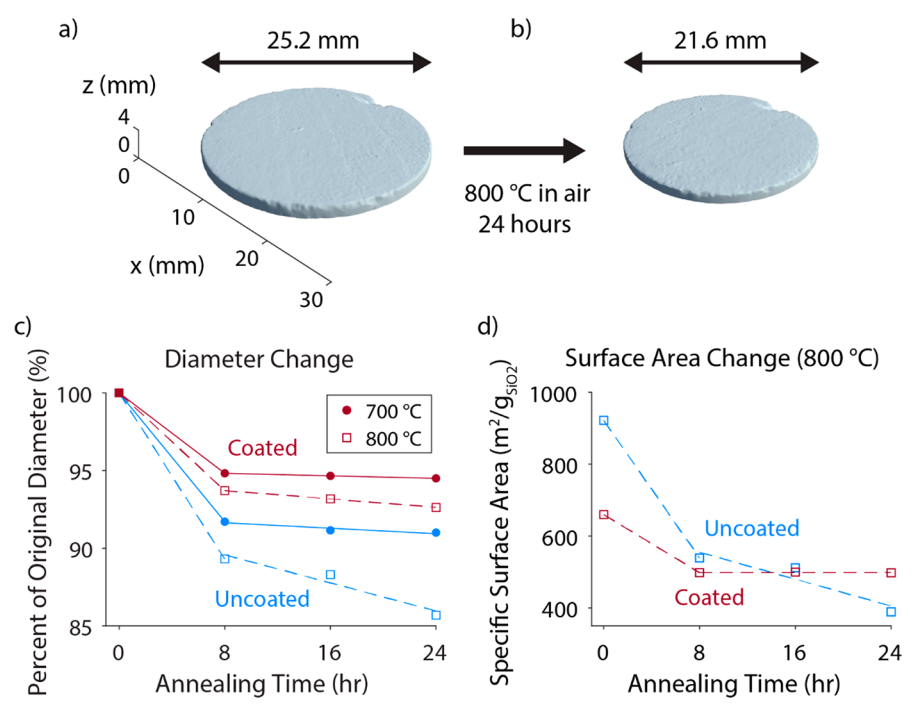


Figure 5. Thermal stability of uncoated and ALD-coated AMs. Bare AM size (a) before and (b) after high-temperature annealing. (c) Changes in the normalized average AM diameter with annealing time in uncoated and fully coated samples. (d) Specific surface area (per gram of silica) with respect to annealing time at 800 °C in uncoated and fully coated samples.

and the total processing time. This approach results in a decrease in the percentage of unreacted precursor (further details in Supplementary Note #15). However, this strategy results in a penalty of increased processing time compared to recipes with short, constant exposure times.

Considering the environmental and economic costs associated with ALD precursor synthesis, high levels of precursor utilization are important to ensure a lean manufacturing process. The percentage of wasted precursor becomes increasingly important at high aspect ratios (because of diffusion limitations) and high surface areas (because of the number of reaction sites). As an example, a single Al₂O₃ cycle on an $80 \times 80 \times 5$ mm³ scaled-up AM with similar material properties would require a minimum of 3.7 g of dosed TMA, amplifying the importance of small changes in the percentage of unreacted precursor. Managing the precursor usage will become even more crucial when considering multiple ALD cycles or more expensive precursors. Although very long processing times can enable low amounts of wasted precursor, such deposition conditions may not be feasible from a throughput standpoint. In manufacturing procesess, the relative marginal cost of these two factors must be evaluated to choose optimal deposition conditions. The model developed in this work will assist in these evaluations.

Implications of Conformal ALD Infiltration. The ability to predict and control ALD infiltration depth into an AM or other ultra-high-aspect-ratio substrate is useful for a wide range of applications. As an example, in the heterogeneous catalysis and thermal insulation fields, structural stability at high temperatures is an important material property. In the case of silica aerogels, densification typically occurs at temperatures beyond 600 °C, which is driven by a minimization of surface energy. This results in a decrease in the AM size and specific surface area, as well as a change in the pore size distribution,

which affects the application potential of these materials beyond 700 $^{\circ}$ C.

A visualization of this densification process in a bare silica AM is shown in Figure 5a,b, where the three-dimensional profile of the AM was measured using focus variation microscopy.⁶⁶ The AM densifies in both the radial and the axial directions after annealing. The densification is tracked with respect to annealing time by measuring the change in the average normalized monolith diameter (Figure 5c). All of the samples shrink significantly after the first 8 h of annealing, but the fully coated AMs contract 38% less at 700 °C and 41% less at 800 °C compared to uncoated samples. When annealing takes place for a further 16 h at 700 °C, the coated AMs show improved long-term stabilization, decreasing in normalized diameter by 0.02%/h, whereas the uncoated AMs decrease by 0.04%/h. At 800 °C, the coated and uncoated AMs contract on average by 0.07%/h and 0.23%/h, respectively. This demonstrates improved thermal stability in the ALD-coated

To further quantify the densification of the AMs, the specific surface area per gram of silica (SSA_{SiO_2}) was measured by BET analysis. SSA_{SiO_2} was quantified as a function of annealing time at 800 °C for both uncoated and conformally coated samples (Figure 5d). Similar results were observed when annealing at 700 °C (Supplementary Note #16). There is an initial decrease in the SSA_{SiO_2} of the coated AM from the ALD process, possibly because of blocking of very small pores. However, after this initial drop, the conformally coated AM is more resistant to high-temperature sintering and subsequent decreases in SSA_{SiO_2} . After 8 h of annealing, the uncoated AM SSA_{SiO_2} decreases by 41%, whereas the coated AM decreases by 17% relative to the uncoated AM. Subsequent annealing up to 24 h yields decreases in SSA_{SiO_2} at an average

rate of 1%/h of the original SSA_{SiO_2} in the uncoated AM, whereas the rate of decrease in the coated AM appears negligible within the resolution capabilities of the BET analysis. Therefore, although the ALD coating results in an initially lower SSA_{SiO_2} , after only 24 h of annealing, the coated AM maintains a higher SSA_{SiO_2} than the uncoated sample. This represents a significant improvement in the high-temperature structural stability of silica aerogels, enabled by conformal ALD Al_2O_3 coatings.

Silica aerogels are composed of a network of interconnected nanoparticles (NPs). Under high-temperature annealing conditions, structural relaxation and NP movement is enabled by decreased NP viscosity. 55 This rearrangement, together with increases in the bulk AM density, result in a decrease in the AM SSA. The improved resistance to SSA degradation in the ALD-coated AMs demonstrates that NP movement is suppressed. This can be attributed to several factors, including decreased surface and/or bulk diffusivity as a result of the ALD coating. Analogous behavior has been observed in studies of applying ALD "overcoats" to heterogeneous catalysts, which enhance sintering resistance at elevated temperatures. 68 Overall, conformal ALD Al₂O₃ coatings enable high-temperature structural stabilization of the AM, both on the macroand nanoscales. This makes conformal ALD modifications on AMs attractive for applications where high-temperature stability of high-surface-area structures is necessary.

CONCLUSIONS

In this work, we demonstrate conformal and saturated ALD coatings on ultra-high-aspect-ratio (>60000:1) silica AMs, based on both SEM/EDS and mass gain measurements. A multidose-QSM procedure, using multiple precursor doses before dosing the counter reactant, was implemented. A model of the ALD coating process was developed and was found to agree with the experimental ALD infiltration depths across multiple sets of conditions, when varying both the exposure time per dose and the number of precursor doses. The model allows for prediction of the total ALD processing time and percentage of unreacted precursor, which are useful for efficient and sustainable manufacturing. Finally, high-temperature structural stabilization enabled by a conformal ALD Al₂O₃ coating is demonstrated under annealing conditions beyond the normal working temperatures for silica aerogels. This helps enable the use of silica aerogels in high-temperature applications such as CST, thermal insulation, and heterogeneous catalysis. Thermal stabilization of silica aerogels using ALD coatings has not been previously demonstrated.

The findings in this work can be used to enable predictable and precursor-efficient ALD of a variety of other materials on ultra-high-aspect-ratio structures. Additionally, the model of the multidose-QSM process allows for controllable ALD infiltration depth, which could be important for informed ALD patterning of AMs or other high-aspect-ratio materials. Equipped with this capability, rationally designed ALD coatings have the potential to address the material property limitations that plague aerogels, including mechanical properties and stability in high-humidity environments. In the future, ALD coatings could also be used to enable multifunctionality, such as electrical conductivity or catalytic activity. Importantly, because of the unique ability of ALD to conformally modify the aerogel surface, well-designed modifications can be

implemented while maintaining the aerogel's unique underlying structure and properties.

EXPERIMENTAL SECTION

Aerogel Monolith Synthesis. AMs were fabricated via sol-gel synthesis, adapted from a previous publication, ⁷⁰ using tetramethylorthosilicate (TMOS, Sigma-Aldrich) with DI water and ammonia (2.0 M in methanol, Sigma-Aldrich) as the catalyst. TMOS solution diluted in methanol was added to an ammonia solution diluted in water, followed by gelation and aging in molds. After several ethanol washes of the wet gel, the AMs were dried using CO₂ critical point drying (Tousimis, model 915B). To remove any remaining contaminants and adsorbed water, the AMs were annealed at 400 °C in air for 24 h. The annealed AMs measured approximately 25 mm in diameter, with thicknesses of 2–3 mm. One side of each AM was slightly concave, whereas the other was slightly convex because of the curvature of the meniscus. The bare AMs had densities of ~0.20 g/cm³, calculated using mass balance and monolith volume measurements.

Atomic Layer Deposition. ALD of Al_2O_3 films on AMs was performed in a custom hot-walled, cross-flow ALD reactor. Trimethylaluminum (TMA, min. 97%, Sigma-Aldrich) and deionized (DI) water were used as ALD precursors. The precursor pneumatic valve actuation times were 2.5 and 1.5 s for TMA and DI water, respectively. The reactor temperature was maintained at 150 °C. Before deposition of Al_2O_3 , the AMs were held at a vacuum pressure of 600 mTorr under constant Ar purging for at least 1 h at 150 °C to ensure the removal of excess water and other adsorbed species.

Prior to coating of the AMs, five DI water precycles, using a multidose-QSM procedure as described here, were performed to ensure reproducible hydroxyl termination on the aerogel surface. The same number of doses were used for TMA and DI water in each coating process. After a controlled exposure time, the ALD chamber was purged with ultra-high-purity Ar (99.999%) with a flow rate of 70 sccm. The purge time was fixed at twice the exposure time. Immediately before the next dose, the Ar flow rate was reduced to 10 sccm to lower the absolute pressure of the chamber and improve the flow of the precursor into the chamber. In the multidose-QSM recipes used in this work, a single precursor was sequentially dosed and purged multiple times before dosing of the counter reactant.

Aerogel Monolith Characterization and Annealing. SEM/EDS maps and line scans were collected using a TESCAN MIRA3 FEG SEM. Cross sections for SEM/EDS measurements were prepared by creating a fracture surface near the middle of the AM after deposition. High-temperature annealing was performed in a Vulcan oven using a ramp rate of 1 °C/min.

BET pore size distribution and surface area were measured using a Micromeritics ASAP 2020 Surface Area and Porosity analyzer. Prior to analysis, the AM samples were degassed at 350 °C (achieved by a ramp of 20 °C/min) for 8 h. BET surface area analysis was conducted at 77 K using the amount of nitrogen adsorbed at various relative vapor pressures between 0.05 < P/P_0 < 0.3. Total pore volume measurements were taken at a relative vapor pressure, P/P_0 , of 0.995. Pore size distributions were calculated using the Barrett–Joyner–Halenda (BJH) method on the desorption branch of the isotherm.

The 3D profiles of AM samples were measured by focus variation microscopy 66 using a Keyence VHS-700 digital microscope. Prior to scanning, both sides of the AM were sanded using 2500 grit SiC sanding paper (Grainger) to make them flat and parallel. The ALD $\rm Al_2O_3$ density was measured using X-ray reflectivity using a Rigaku SmartLab X-ray Diffractometer. GlobalFit 2 Rigaku software version 2.0.10.0 was used to analyze the data and extract the film density.

ASSOCIATED CONTENT

Supporting Information

The Supporting Information is available free of charge at https://pubs.acs.org/doi/10.1021/acs.chemmater.1c00770.

Example pressure profiles during a multidose-QSM recipe, AM sample preparation and characterization, expected ALD mass gain and atomic percentage, TMA saturation dose calculations, measured ALD infiltration depths, model parameters, model assumptions, and justifications, model of initial precursor diffusion to the ALD reaction front, modeled precursor partial pressure using various ALD conditions, model of varying exposure time per dose with dose number, tortuosity sensitivity analysis, BET data after annealing at 700 °C, and estimated time for AMs to reach thermal equilibrium with the ALD chamber (PDF)

AUTHOR INFORMATION

Corresponding Authors

Andrej Lenert – Department of Chemical Engineering, University of Michigan, Ann Arbor, Michigan 48109, United States; ocid.org/0000-0002-1142-6627;

Email: alenert@umich.edu

Neil P. Dasgupta — Department of Mechanical Engineering, University of Michigan, Ann Arbor, Michigan 48109, United States; Department of Materials Science and Engineering, University of Michigan, Ann Arbor, Michigan 48109, United States; orcid.org/0000-0002-5180-4063; Email: ndasgupt@umich.edu

Authors

Andrew J. Gayle – Department of Mechanical Engineering, University of Michigan, Ann Arbor, Michigan 48109, United States

Zachary J. Berquist — Department of Chemical Engineering, University of Michigan, Ann Arbor, Michigan 48109, United States

Yuxin Chen – Department of Mechanical Engineering, University of Michigan, Ann Arbor, Michigan 48109, United States

Alexander J. Hill – Department of Chemical Engineering, University of Michigan, Ann Arbor, Michigan 48109, United States

Jacob Y. Hoffman – Department of Chemical Engineering, University of Michigan, Ann Arbor, Michigan 48109, United States

Ashley R. Bielinski — Department of Mechanical Engineering, University of Michigan, Ann Arbor, Michigan 48109, United States

Complete contact information is available at: https://pubs.acs.org/10.1021/acs.chemmater.1c00770

Author Contributions

*A.J.G. and Z.J.B. contributed equally to this work.

Notes

The authors declare the following competing financial interest(s): The authors have filed a provisional patent application related to this work.

ACKNOWLEDGMENTS

This material is based upon work supported by the U.S. Department of Energy's Office of Energy Efficiency and Renewable Energy (EERE) under Solar Energy Technologies Office Award Number DE-EE0008526 and DE-EE0009376. The view expressed herein do not necessarily represent the view of the U.S. Department of Energy or the United States

Government. This work is supported by the National Science Foundation under Grant No. 1751590. A.J.G. and Z.J.B. acknowledge support from the National Science Foundation Graduate Research Fellowship Program under Grant No. DGE-1256260. Z.J.B. also acknowledges support from the University of Michigan Dow Sustainability Doctoral Research Fellowship. The SEM/EDS work was performed at the Michigan Center for Materials Characterization and aerogel synthesis was performed in part at the Lurie Nanofabrication Facility, which are supported by the College of Engineering at the University of Michigan. We acknowledge Tae H. Cho for help with the X-ray reflectivity measurements.

REFERENCES

- (1) Hrubesh, L. W. Aerogel Applications. J. Non-Cryst. Solids 1998, 225, 335-342.
- (2) Pierre, A. C. History of Aerogels. In *Aerogels Handbook*; Aegerter, M. A., Leventis, N., Koebel, M. M., Eds.; Springer: New York, 2011; pp 3–18.
- (3) Amonette, J. E.; Matyáš, J. Functionalized Silica Aerogels for Gas-Phase Purification, Sensing, and Catalysis: A Review. *Microporous Mesoporous Mater.* **2017**, 250, 100–119.
- (4) Rubin, M.; Lampert, C. M. Transparent Silica Aerogels for Window Insulation. *Sol. Energy Mater.* **1983**, 7 (4), 393–400.
- (5) Nemoto, J.; Saito, T.; Isogai, A. Simple Freeze-Drying Procedure for Producing Nanocellulose Aerogel-Containing, High-Performance Air Filters. ACS Appl. Mater. Interfaces 2015, 7 (35), 19809–19815.
- (6) Cantin, M.; Casse, M.; Koch, L.; Jouan, R.; Mestreau, P.; Roussel, D.; Bonnin, F.; Moutel, J.; Teichner, S. J. Silica Aerogels Used as Cherenkov Radiators. *Nucl. Instrum. Methods* **1974**, *118* (1), 177–182.
- (7) Cui, S.; Liu, Y.; Fan, M. H.; Cooper, A. T.; Lin, B. L.; Liu, X. Y.; Han, G. F.; Shen, X. D. Temperature Dependent Microstructure of MTES Modified Hydrophobic Silica Aerogels. *Mater. Lett.* **2011**, *65* (4), 606–609.
- (8) Tamon, H.; Sone, T.; Mikami, M.; Okazaki, M. Preparation and Characterization of Silica Titania and Silica Alumina Aerogels. *J. Colloid Interface Sci.* **1997**, *188* (2), 493–500.
- (9) Cremers, V.; Puurunen, R. L.; Dendooven, J. Conformality in Atomic Layer Deposition: Current Status Overview of Analysis and Modelling. *Appl. Phys. Rev.* **2019**, *6* (2), 021302.
- (10) George, S. M. Atomic Layer Deposition: An Overview. *Chem. Rev.* **2010**, *110* (1), 111–131.
- (11) Li, H.; Gao, Y.; Shao, Y.; Su, Y.; Wang, X. Vapor-Phase Atomic Layer Deposition of Co9S8 and Its Application for Supercapacitors. *Nano Lett.* **2015**, *15* (10), 6689–6695.
- (12) Kazyak, E.; Chen, K. H.; Wood, K. N.; Davis, A. L.; Thompson, T.; Bielinski, A. R.; Sanchez, A. J.; Wang, X.; Wang, C.; Sakamoto, J.; Dasgupta, N. P. Atomic Layer Deposition of the Solid Electrolyte Garnet Li7La3Zr2O12. *Chem. Mater.* **2017**, 29 (8), 3785–3792.
- (13) Elam, J. W.; Routkevitch, D.; Mardilovich, P. P.; George, S. M. Conformal Coating on Ultrahigh-Aspect-Ratio Nanopores of Anodic Alumina by Atomic Layer Deposition. *Chem. Mater.* **2003**, *15* (18), 3507–3517.
- (14) Bachmann, J.; Jing, J.; Knez, M.; Barth, S.; Shen, H.; Mathur, S.; Gösele, U.; Nielsch, K. Ordered Iron Oxide Nanotube Arrays of Controlled Geometry and Tunable Magnetism by Atomic Layer Deposition. J. Am. Chem. Soc. 2007, 129 (31), 9554–9555.
- (15) Shin, H.; Jeong, D. K.; Lee, J.; Sung, M. M.; Kim, J. Formation of TiO2 and ZrO2 Nanotubes Using Atomic Layer Deposition with Ultraprecise Control of the Wall Thickness. *Adv. Mater.* **2004**, *16* (14), 1197–1200.
- (16) Dasgupta, N. P.; Liu, C.; Andrews, S.; Prinz, F. B.; Yang, P. Atomic Layer Deposition of Platinum Catalysts on Nanowire Surfaces for Photoelectrochemical Water Reduction. *J. Am. Chem. Soc.* **2013**, 135 (35), 12932–12935.
- (17) Dasgupta, N. P.; Jung, H. J.; Trejo, O.; McDowell, M. T.; Hryciw, A.; Brongersma, M.; Sinclair, R.; Prinz, F. B. Atomic Layer

- Deposition of Lead Sulfide Quantum Dots on Nanowire Surfaces. *Nano Lett.* **2011**, *11* (3), 934–940.
- (18) Min, Y. S.; Bae, E. J.; Jeong, K. S.; Cho, Y. J.; Lee, J. H.; Choi, W. B.; Park, G. S. Ruthenium Oxide Nanotube Arrays Fabricated by Atomic Layer Deposition Using a Carbon Nanotube Template. *Adv. Mater.* **2003**, *15* (12), 1019–1022.
- (19) Yim, J.; Ylivaara, O. M. E.; Ylilammi, M.; Korpelainen, V.; Haimi, E.; Verkama, E.; Utriainen, M.; Puurunen, R. L. Saturation Profile Based Conformality Analysis for Atomic Layer Deposition: Aluminum Oxide in Lateral High-Aspect-Ratio Channels. *Phys. Chem. Chem. Phys.* **2020**, 22 (40), 23107–23120.
- (20) Ylılammi, M.; Ylıvaara, O. M. E.; Puurunen, R. L. Modeling Growth Kinetics of Thin Films Made by Atomic Layer Deposition in Lateral High-Aspect-Ratio Structures. *J. Appl. Phys.* **2018**, *123* (20), 205301.
- (21) Miikkulainen, V.; Leskelä, M.; Ritala, M.; Puurunen, R. L. Crystallinity of Inorganic Films Grown by Atomic Layer Deposition: Overview and General Trends. *J. Appl. Phys.* **2013**, *113* (2), 021301.
- (22) Database of ALD processes https://www.atomiclimits.com/alddatabase/ (accessed 2021-01-04).
- (23) Kucheyev, S. O.; Biener, J.; Wang, Y. M.; Baumann, T. F.; Wu, K. J.; van Buuren, T.; Hamza, A. V.; Satcher, J. H.; Elam, J. W.; Pellin, M. J. Atomic Layer Deposition of ZnO on Ultralow-Density Nanoporous Silica Aerogel Monoliths. *Appl. Phys. Lett.* **2005**, *86*, 083108.
- (24) Hamann, B. T. W.; Martinson, A. B. F.; Elam, J. W.; Pellin, M. J.; Hupp, J. T. Aerogel Templated ZnO Dye-Sensitized Solar Cells. *Adv. Mater.* **2008**, 20 (8), 1560–1564.
- (25) Li, T. C.; Fabregat-Santiago, F.; Farha, O. K.; Spokoyny, A. M.; Raga, S. R.; Bisquert, J.; Mirkin, C. A.; Marks, T. J.; Hupp, J. T. SiO2 Aerogel Templated, Porous TiO2 Photoanodes for Enhanced Performance in Dye-Sensitized Solar Cells Containing a Ni (III)/(IV) Bis (Dicarbollide) Shuttle. *J. Phys. Chem. C* **2011**, *115* (22), 11257–11264.
- (26) Williams, V. O.; Jeong, N. C.; Prasittichai, C.; Farha, O. K.; Pellin, M. J.; Hupp, J. T. Fast Transporting ZnO-TiO2 Coaxial Photoanodes for Dye-Sensitized Solar Cells Based on ALD-Modified SiO2 Aerogel Frameworks. *ACS Nano* **2012**, *6* (7), 6185–6196.
- (27) Yu, M.; Wang, A.; Wang, Y.; Li, C.; Shi, G. An Alumina Stabilized ZnO-Graphene Anode for Lithium Ion Batteries via Atomic Layer Deposition. *Nanoscale* **2014**, *6* (19), 11419–11424.
- (28) Yu, M.; Wang, A.; Tian, F.; Song, H.; Wang, Y.; Li, C.; Hong, J. D.; Shi, G. Dual-Protection of a Graphene-Sulfur Composite by a Compact Graphene Skin and an Atomic Layer Deposited Oxide Coating for a Lithium-Sulfur Battery. *Nanoscale* **2015**, *7* (12), 5292–5298.
- (29) Fleischmann, S.; Leistenschneider, D.; Lemkova, V.; Krüner, B.; Zeiger, M.; Borchardt, L.; Presser, V. Tailored Mesoporous Carbon/Vanadium Pentoxide Hybrid Electrodes for High Power Pseudocapacitive Lithium and Sodium Intercalation. *Chem. Mater.* **2017**, 29 (20), 8653–8662.
- (30) Korhonen, J. T.; Kettunen, M.; Ras, R. H. A.; Ikkala, O. Hydrophobic Nanocellulose Aerogels as Floating, Sustainable, Reusable, and Recyclable Oil Absorbents. *ACS Appl. Mater. Interfaces* **2011**, 3 (6), 1813–1816.
- (31) Lu, J.; Li, Y.; Song, W.; Losego, M. D.; Monikandan, R.; Jacob, K. I.; Xiao, R. Atomic Layer Deposition onto Thermoplastic Polymeric Nanofibrous Aerogel Templates for Tailored Surface Properties. ACS Nano 2020, 14 (7), 7999–8011.
- (32) King, J. S.; Wittstock, A.; Biener, J.; Kucheyev, S. O.; Wang, Y. M.; Baumann, T. F.; Giri, S. K.; Hamza, A. V.; Baeumer, M.; Bent, S. F. Ultralow Loading Pt Nanocatalysts Prepared by Atomic Layer Deposition on Carbon Aerogels. *Nano Lett.* **2008**, *8* (8), 2405–2409.
- (33) Mi, Y.; Wen, L.; Wang, Z.; Cao, D.; Zhao, H.; Zhou, Y.; Grote, F.; Lei, Y. Ultra-Low Mass Loading of Platinum Nanoparticles on Bacterial Cellulose Derived Carbon Nanofibers for Efficient Hydrogen Evolution. *Catal. Today* **2016**, 262, 141–145.
- (34) Khalily, M. A.; Eren, H.; Akbayrak, S.; Susapto, H. H.; Biyikli, N.; Özkar, S.; Guler, M. O. Facile Synthesis of Three-Dimensional Pt-

- TiO2 Nano-Networks: A Highly Active Catalyst for the Hydrolytic Dehydrogenation of Ammonia-Borane. *Angew. Chem., Int. Ed.* **2016**, 55 (40), 12257–12261.
- (35) Justh, N.; Mikula, G. J.; Bakos, L. P.; Nagy, B.; Laszlo, K.; Parditka, B.; Erdélyi, Z.; Takáts, V.; Mizsei, J.; Szilágyi, I. M. Photocatalytic Properties of TiO2@polymer and TiO2@carbon Aerogel Composites Prepared by Atomic Layer Deposition. *Carbon* 2019, 147, 476–482.
- (36) Bakos, L. P.; Mensah, J.; László, K.; Parditka, B.; Erdélyi, Z.; Székely, E.; Lukács, I.; Kónya, Z.; Cserháti, C.; Zhou, C.; Seo, J. W.; Halasi, G.; Szilágyi, I. M. Nitrogen Doped Carbon Aerogel Composites with TiO2 and ZnO Prepared by Atomic Layer Deposition. J. Mater. Chem. C 2020, 8 (20), 6891–6899.
- (37) Wu, J.; Zhu, X.; Shapiro, D. A.; Lee, J. R. I.; Van Buuren, T.; Biener, M. M.; Gammon, S. A.; Li, T. T.; Baumann, T. F.; Hitchcock, A. P. Four-Dimensional Imaging of ZnO-Coated Alumina Aerogels by Scanning Transmission X-Ray Microscopy and Ptychographic Tomography. J. Phys. Chem. C 2018, 122 (44), 25374–25385.
- (38) Mane, A. U.; Greene, J. P.; Nolen, J. A.; Sampathkumaran, U.; Owen, T. W.; Winter, R.; Elam, J. W. Refractory Nanoporous Materials Fabricated Using Tungsten Atomic Layer Deposition on Silica Aerogels. *Appl. Surf. Sci.* **2012**, 258 (17), 6472–6478.
- (39) Kucheyev, S. O.; Biener, J.; Baumann, T. F.; Wang, Y. M.; Hamza, A. V.; Li, Z.; Lee, D. K.; Gordon, R. G. Mechanisms of Atomic Layer Deposition on Substrates with Ultrahigh Aspect Ratios. *Langmuir* **2008**, *24* (3), 943–948.
- (40) Smith, S. W.; Buesch, C.; Matthews, D. J.; Simonsen, J.; Conley, J. F. Improved Oxidation Resistance of Organic/Inorganic Composite Atomic Layer Deposition Coated Cellulose Nanocrystal Aerogels. J. Vac. Sci. Technol., A 2014, 32 (4), 041508.
- (41) Gordon, R. G.; Hausmann, D.; Kim, E.; Shepard, J. A Kinetic Model for Step Coverage by Atomic Layer Deposition in Narrow Holes or Trenches. *Chem. Vap. Deposition* **2003**, *9* (2), 73–78.
- (42) Dendooven, J.; Deduytsche, D.; Musschoot, J.; Vanmeirhaeghe, R. L.; Detavernier, C. Modeling the Conformality of Atomic Layer Deposition: The Effect of Sticking Probability. *J. Electrochem. Soc.* **2009**, *156* (4), P63.
- (43) Yanguas-Gil, A.; Elam, J. W. Self-Limited Reaction-Diffusion in Nanostructured Substrates: Surface Coverage Dynamics and Analytic Approximations to ALD Saturation Times. *Chem. Vap. Deposition* **2012**, *18* (1–3), 46–52.
- (44) Poodt, P.; Mameli, A.; Schulpen, J.; Kessels, W. M. M.; Roozeboom, F. Effect of Reactor Pressure on the Conformal Coating inside Porous Substrates by Atomic Layer Deposition. *J. Vac. Sci. Technol., A* **2017**, 35 (2), 021502.
- (45) Adomaitis, R. A. A Ballistic Transport and Surface Reaction Model for Simulating Atomic Layer Deposition Processes in High-Aspect-Ratio Nanopores. *Chem. Vap. Deposition* **2011**, *17* (10–12), 353–365.
- (46) Lankhorst, A. M.; Paarhuis, B. D.; Terhorst, H. J. C. M.; Simons, P. J. P. M.; Kleijn, C. R. Transient ALD Simulations for a Multi-Wafer Reactor with Trenched Wafers. *Surf. Coat. Technol.* **2007**, 201 (22–23), 8842–8848.
- (47) Miyano, Y.; Narasaki, R.; Ichikawa, T.; Fukumoto, A.; Aiso, F.; Tamaoki, N. Multiscale Modeling for SiO2 Atomic Layer Deposition for High-Aspect-Ratio Hole Patterns. *Jpn. J. Appl. Phys.* **2018**, *57*, 06JB03.
- (48) Yanguas-Gil, A.; Elam, J. W. A Markov Chain Approach to Simulate Atomic Layer Deposition Chemistry and Transport inside Nanostructured Substrates. *Theor. Chem. Acc.* **2014**, *133*, 1465.
- (49) Yanguas-Gil, A. Thin Film Growth in Nanostructured Materials. In *Growth and Transport in Nanostructured Materials:* Reactive Transport in PVD, CVD, and ALD; Springer: 2017; pp 69–99.
- (50) Jin, W.; van Ommen, J. R.; Kleijn, C. R. Moving Reaction Fronts in Fractal Nanoparticle Agglomerates. *Chem. Eng. Sci.* **2019**, 206. 180–186.
- (51) Grillo, F.; Kreutzer, M. T.; van Ommen, J. R. Modeling the Precursor Utilization in Atomic Layer Deposition on Nanostructured

Materials in Fluidized Bed Reactors. Chem. Eng. J. 2015, 268, 384–398.

- (52) Zazpe, R.; Sopha, H.; Prikryl, J.; Krbal, M.; Mistrik, J.; Dvorak, F.; Hromadko, L.; Macak, J. M. A 1D Conical Nanotubular TiO2/CdS Heterostructure with Superior Photon-to-Electron Conversion. *Nanoscale* **2018**, *10* (35), 16601–16612.
- (53) Chen, H.; Lin, Q.; Xu, Q.; Yang, Y.; Shao, Z.; Wang, Y. Plasma Activation and Atomic Layer Deposition of TiO2 on Polypropylene Membranes for Improved Performances of Lithium-Ion Batteries. *J. Membr. Sci.* **2014**, *458*, 217–224.
- (54) Kim, I. S.; Borycz, J.; Platero-Prats, A. E.; Tussupbayev, S.; Wang, T. C.; Farha, O. K.; Hupp, J. T.; Gagliardi, L.; Chapman, K. W.; Cramer, C. J.; Martinson, A. B. F. Targeted Single-Site MOF Node Modification: Trivalent Metal Loading via Atomic Layer Deposition. *Chem. Mater.* **2015**, *27* (13), 4772–4778.
- (55) Strobach, E.; Bhatia, B.; Yang, S.; Zhao, L.; Wang, E. N. High Temperature Stability of Transparent Silica Aerogels for Solar Thermal Applications High Temperature Stability of Transparent Silica Aerogels for Solar Thermal Applications. *APL Mater.* **2019**, 7 (8), 081104.
- (56) Leng, C. Z.; Losego, M. D. Vapor Phase Infiltration (VPI) for Transforming Polymers into Organic-Inorganic Hybrid Materials: A Critical Review of Current Progress and Future Challenges. *Mater. Horiz.* **2017**, 4 (5), 747–771.
- (57) Akyildiz, H. I.; Padbury, R. P.; Parsons, G. N.; Jur, J. S. Temperature and Exposure Dependence of Hybrid Organic-Inorganic Layer Formation by Sequential Vapor Infiltration into Polymer Fibers. *Langmuir* **2012**, 28 (44), 15697–15704.
- (58) Gong, B.; Peng, Q.; Jur, J. S.; Devine, C. K.; Lee, K.; Parsons, G. N. Sequential Vapor Infiltration of Metal Oxides into Sacrificial Polyester Fibers: Shape Replication and Controlled Porosity of Microporous/Mesoporous Oxide Monoliths. *Chem. Mater.* **2011**, 23 (15), 3476–3485.
- (59) Gregorczyk, K. E.; Pickup, D. F.; Sanz, M. G.; Irakulis, I. A.; Rogero, C.; Knez, M. Tuning the Tensile Strength of Cellulose through Vapor-Phase Metalation. *Chem. Mater.* **2015**, 27 (1), 181–188.
- (60) Sønsteby, H. H.; Yanguas-Gil, A.; Elam, J. W. Consistency and Reproducibility in Atomic Layer Deposition. *J. Vac. Sci. Technol., A* **2020**, 38 (2), 020804.
- (61) Lee, H. Y.; An, C. J.; Piao, S. J.; Ahn, D. Y.; Kim, M. T.; Min, Y. S. Shrinking Core Model for Knudsen Diffusion-Limited Atomic Layer Deposition on a Nanoporous Monolith with an Ultrahigh Aspect Ratio. *J. Phys. Chem. C* **2010**, *114* (43), 18601–18606.
- (62) Clausing Factors. In *Handbook of Vacuum Science and Technology*; Hoffman, D., Singh, B., Thomas III, J., Eds.; Academic: San Diego, 1997; pp 38–39.
- (63) Barrande, M.; Bouchet, R.; Denoyel, R. Tortuosity of Porous Particles. *Anal. Chem.* **200**7, *79* (23), 9115–9121.
- (64) Mueller, R.; Zhang, S.; Klink, M.; Bäumer, M.; Vasenkov, S. The Origin of a Large Apparent Tortuosity Factor for the Knudsen Diffusion inside Monoliths of a Samaria-Alumina Aerogel Catalyst: A Diffusion NMR Study. *Phys. Chem. Chem. Phys.* **2015**, *17* (41), 27481–27487.
- (65) Reichenauer, G.; Stumpf, C.; Fricke, J. Characterization of SiO2, RF and Carbon Aerogels by Dynamic Gas Expansion. *J. Non-Cryst. Solids* **1995**, *186*, 334–341.
- (66) Optical Measurement of Surface Topography; Leach, R., Ed.; Springer-Verlag: Berlin, 2011.
- (67) Mane, A. U.; Greene, J. P.; Nolen, J. A.; Sampathkumaran, U.; Owen, T. W.; Winter, R.; Elam, J. W. Applied Surface Science Refractory Nanoporous Materials Fabricated Using Tungsten Atomic Layer Deposition on Silica Aerogels. *Appl. Surf. Sci.* **2012**, 258 (17), 6472–6478.
- (68) O'Neill, B. J.; Jackson, D. H. K.; Lee, J.; Canlas, C.; Stair, P. C.; Marshall, C. L.; Elam, J. W.; Kuech, T. F.; Dumesic, J. A.; Huber, G. W. Catalyst Design with Atomic Layer Deposition. *ACS Catal.* **2015**, 5 (3), 1804–1825.

- (69) Elam, J. W.; Libera, J. A.; Pellin, M. J.; Stair, P. C. Spatially Controlled Atomic Layer Deposition in Porous Materials. *Appl. Phys. Lett.* **2007**, *91* (24), 243105.
- (70) Berquist, Z. J.; Turaczy, K. K.; Lenert, A. Plasmon-Enhanced Greenhouse Selectivity for High-Temperature Solar Thermal Energy Conversion. *ACS Nano* **2020**, *14* (10), 12605–12613.
- (71) Dasgupta, N. P.; Mack, J. F.; Langston, M. C.; Bousetta, A.; Prinz, F. B. Design of an Atomic Layer Deposition Reactor for Hydrogen Sulfide Compatibility. *Rev. Sci. Instrum.* **2010**, *81* (4), 044102.